Geochemistry Geophysics Geosystems G3

Article
Volume 12, Number 10
14 October 2011
Q10007, doi:10.1029/2011GC003759
ISSN: 1525-2027

Published by AGU and the Geochemical Society

Cascadia tremor spectra: Low corner frequencies and earthquake-like high-frequency falloff

Jian Zhang
Scripps Institution of Oceanography, University of California, San Diego, 9500 Gilman Drive, La Jolla, California 92093-0238, USA

Now at Los Alamos National Laboratory, Los Alamos, New Mexico 87545, USA (jjzhang@lanl.gov)

Peter Gerstoft, Peter M. Shearer, and Huajian Yao
Scripps Institution of Oceanography, University of California, San Diego, 9500 Gilman Drive, La Jolla, California 92093-0238, USA

John E. Vidale, Heidi Houston, and Abhijit Ghosh
Department of Earth and Space Sciences, University of Washington, 4000 15th Avenue NE, Seattle, Washington 98195-1310, USA

[1] The discovery of non-volcanic tremor (NVT) has opened a new window to observe major Earth plate boundaries. However, the spectral characteristics of NVT have not been well studied due to poor signal-to-noise ratio (SNR) on individual seismograms. We estimate the spectral content of Cascadia tremor between 2.5 and 20 Hz by suppressing noise using array analysis, and compute empirical path corrections using nearby small earthquakes. We demonstrate that the displacement spectra of the Cascadia tremor have corner frequencies around 3–8 Hz and fall off at f^{-2} to f^{-3} at higher frequencies. Our results have the following implications. (1) The high-frequency falloff of tremor agrees with the observations of regular earthquakes, suggesting that tremor can be analyzed using standard spectral models. Prior analyses that have shown a tremor spectral falloff proportional to f^{-1} may reflect only the spectral behavior over a limited frequency band. (2) Tremor may be no different from a swarm of microearthquakes with abnormally small stress drops on the order of kPa, likely due to the presence of fluids. Alternatively the low corner frequencies of tremor may reflect abnormally slow ruptures. (3) Fitting a standard *Brune* (1970) spectral model implies a moment release rate of Cascadia tremor of 3.8×10^{10} N·m/s assuming the tremor signals are *P* waves (or 1.4×10^{10} N·m/s assuming *S*-waves). This implies that a typical 20-day long tremor episode releases moment equivalent to Mw 5.1 (*P*-wave) or Mw 4.9 (*S*-wave), although these may be underestimates if the spectra deviate substantially from the *Brune* model at very low frequencies.

Components: 4900 words, 12 figures.

Keywords: beamforming; source spectrum; tremor.

Index Terms: 7215 Seismology: Earthquake source observations (1240); 7240 Seismology: Subduction zones (1207, 1219, 1240); 8118 Tectonophysics: Dynamics and mechanics of faulting (8004).

Received 15 June 2011; **Revised** 2 September 2011; **Accepted** 2 September 2011; **Published** 14 October 2011.

Zhang, J., P. Gerstoft, P. M. Shearer, H. Yao, J. E. Vidale, H. Houston, and A. Ghosh (2011), Cascadia tremor spectra: Low corner frequencies and earthquake-like high-frequency falloff, *Geochem. Geophys. Geosyst.*, *12*, Q10007, doi:10.1029/2011GC003759.

1. Introduction

[2] The discovery of non-volcanic tremor (NVT) [*Obara*, 2002; *Rogers and Dragert*, 2003] has opened a new window for Earth scientists to model and understand plate boundary dynamics. The spectral characteristics of NVT contain important information about the physical fault processes controlling episodic tremor and slip (ETS) and shed light on the manifestations of seismic slip from slow events to mega earthquakes [*Peng and Gomberg*, 2010; *Beroza and Ide*, 2011]. Prior tremor analyses have mainly focused on frequencies of 1–10 Hz and suggested a high-frequency falloff proportional to frequency [*Ide et al.*, 2007; *Shelly et al.*, 2007; *Rubinstein et al.*, 2007] rather than the frequency squared commonly observed for regular earthquakes. However, an f^{-1} falloff would be puzzling because the radiated energy remains finite only if the displacement spectrum falls off at least as fast as $f^{-1.5}$ in the asymptotic limit at high frequencies [*Lee et al.*, 2003].

[3] Given these issues, a key to understanding tremor is to extend tremor spectral observations to higher frequencies so that the falloff rates and associated corner frequencies can be estimated with greater resolution. Studies of tremor focusing at higher frequencies [*Guilhem et al.*, 2010] are rare in literature. In general measuring tremor amplitudes at high frequencies is challenging because of the typically poor signal-to-noise ratio (SNR) of the tremor records. When seismic array data are available, beamforming [e.g., *Gerstoft et al.*, 2008] can suppress noise to isolate the coherent tremor signal, which enables measuring tremor spectra with greater resolution and to higher frequencies than can be observed from single-station data. In this paper we analyze tremor spectra using beamforming and demonstrate that Cascadia tremor show earthquake-like high-frequency spectral falloff rates at f^{-2} to f^{-3} and have corner frequencies around 3–8 Hz.

2. Method: Array Beamforming

[4] Frequency domain beamforming allows source spectra and locations to be estimated from the peak beamformer power. In the frequency domain the seismic displacement records are ordered into an N-dimensional vector $\mathbf{v}(\omega)$. Assuming a plane wave response $\mathbf{w}(\omega) = \exp(i\omega s\mathbf{re})$, where s is slowness, $\mathbf{r}$ describes the coordinates of the array relative to the array center and $\mathbf{e}$ contains the direction cosines of the plane wave for a given azimuth θ. The beamformer output is then given by $b(\omega, s, \theta) = \frac{1}{N}\mathbf{w}^H\mathbf{C}\mathbf{w}$, where $\mathbf{C}(\omega)$ is the cross-spectral density matrix (CSDM) given by: $\mathbf{C}(\omega) = E(\mathbf{v}\mathbf{v}^H)$. Beamforming can also be related to the array response to point sources at the plate boundary that shoot rays up to the sensors. Given $\mathbf{w}(\omega, lat, lon) = \exp(i\omega\,\mathbf{t}_{lat,lon})$, where $\mathbf{t}_{lat,lon}$ describes the travel-time estimates from a grid point to each sensor, using a local travel-time and plate boundary model. The beamformer output is then given by $b(\omega, lat, lon) = \frac{1}{N}\mathbf{w}^H(\omega, lat, lon)\mathbf{C}(\omega)\mathbf{w}(\omega, lat, lon)$. This allows the tremor source locations to be found where they best match the beamformer output.

[5] We assume a simple linear signal model $\mathbf{v}(\omega) = S(\omega)p(\omega)\Psi(\omega) + \mathbf{n}(\omega)$, where $S(\omega)$ is the source strength of the coherent signal, $p(\omega)$ is the average transmission term from the source to the sensors, $\Psi(\omega)$ represents the different arrival phases at each sensor, and $\mathbf{n}$ is the noise at each sensor, which is assumed Gaussian distributed with zero mean and diagonal covariance $\sigma^2\mathbf{I}$, i.e., the noise is identical and independently distributed. Using this statistical model the average power spectra $P(\omega)$ and the cross-spectral density matrix (CSDM) $\mathbf{C}(\omega)$ are given by:

$$\begin{cases} P(\omega) = \frac{1}{N}E(\mathbf{v}^H\mathbf{v}) = S^2p^2 + \sigma^2 \\ \mathbf{C}(\omega) = E(\mathbf{v}\mathbf{v}^H) = S^2p^2\Psi\Psi^H + \sigma^2\mathbf{I} \end{cases} \quad (1)$$

For earthquakes it is assumed that $S^2\,p^2 \gg \sigma^2$, whereby σ^2 can be neglected and to estimate S we correct $P(\omega)$ for the average propagation path p. For tremor, however, $S^2p^2 \approx \sigma^2$, and for higher frequencies noise can be dominating. This makes it difficult to estimate S directly from the $P(\omega)$. Here we show how beamforming can be used to estimate the tremor source power.

[6] Taking the form of $\mathbf{C}(\omega)$ in equation (1), the beamformer power is then given by

$$b(\omega, s, \theta) = \frac{1}{N}\mathbf{w}^H\mathbf{C}\mathbf{w} = \frac{1}{N}\left(S^2p^2\mathbf{w}^H\Psi\Psi^H\mathbf{w} + N\sigma^2\right) \quad (2)$$

At the optimal point (s^{tre}, θ^{tre}) from the tremor, $\mathbf{w}(s^{tre}, \theta^{tre}) = \Psi$, also $\Psi^H\Psi = N$, whereby

$$\begin{aligned} b(\omega, s^{tre}, \theta^{tre}) &= \frac{1}{N}\mathbf{w}^H\mathbf{C}\mathbf{w} = \frac{1}{N}S^2p^2\left|\Psi^H\Psi\right|^2 + \sigma^2 \\ &= S^2p^2N + \sigma^2 = P + S^2p^2(N-1) \end{aligned} \quad (3)$$

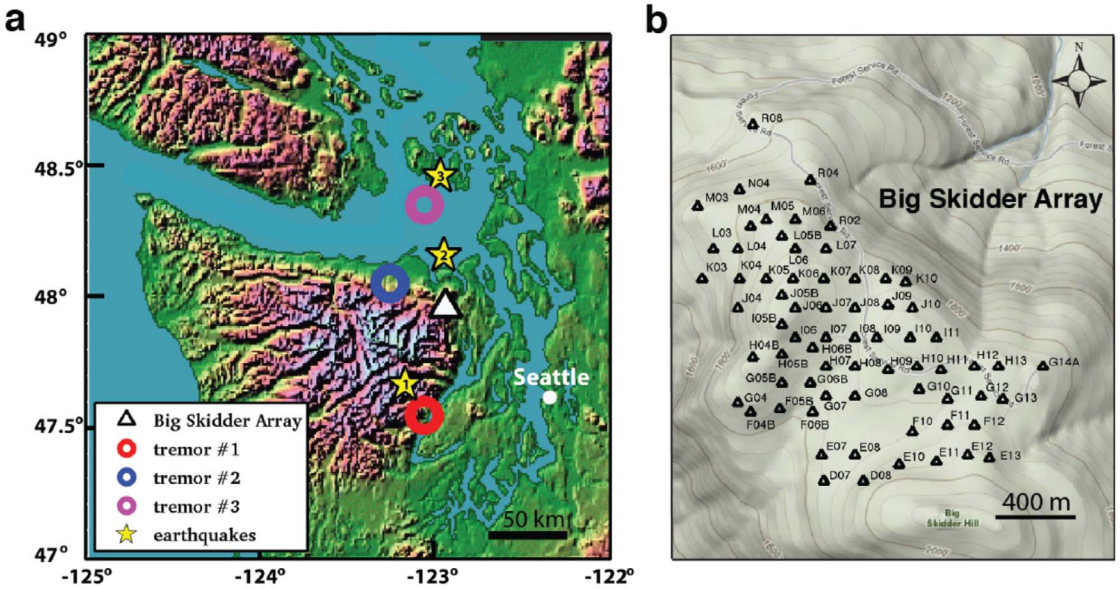

Figure 1. Locations of the Big Skidder array, three typical Cascadia tremor bursts, and their nearby earthquakes. (a) Map view. We focus on three tremor bursts: (1) May 8 03:39–03:52; (2) May 9 03:00–04:00; and (3) May 12 11:50–12:50, which are each close to one of three local earthquakes. (b) Geometry of the Big Skidder array.

The tremor source strength S can then be estimated from the difference between the peak beamformer output $b(\omega, s^{tre}, \theta^{tre})$ and the average power $\mathrm{P}(\omega)$, i.e.,

$$S^2 p^2 = \frac{1}{(\mathrm{N}-1)}\left(b(\omega, s^{tre}, \theta^{tre}) - \mathrm{P}(\omega)\right) \tag{4}$$

where the transmission loss p^2 can be estimated using small local earthquakes and numerical modeling. Thus, equation (4) corresponds to traditional beamforming without the diagonal of the CSDM [e.g., *Brooks and Humphreys*, 2006; *Harmon et al.*, 2010].

[7] In practice the $\mathrm{P}(\omega)$ and the $\mathbf{C}(\omega)$ are estimated by forming ensemble averages over M snapshots, i.e., $\hat{\mathrm{P}}(\omega) = \frac{1}{\mathrm{NM}}\sum_{m=1}^{\mathrm{M}} \mathbf{v}_m^{\mathrm{H}}\mathbf{v}_m$ and $\hat{\mathbf{C}}(\omega) = \frac{1}{\mathrm{M}}\sum_{m=1}^{\mathrm{M}} \mathbf{v}_m\mathbf{v}_m^{\mathrm{H}}$, noting that $\mathrm{N}\hat{\mathrm{P}}(\omega) = \mathrm{tr}(\hat{\mathbf{C}}(\omega))$.

3. Data Processing and Analysis

[8] The Cascadia tremor activity during the main ETS event from May 5 to 21, 2008 was recorded at a dense array of ~100 short-period vertical-component sensors deployed at Big Skidder Hill, WA (Figure 1). For each sensor we first split the time domain signals (sampling frequency 100 Hz) into 3-s time snapshots, then transform the signals into the frequency domain and remove the instrument response. The beamformer output is averaged over the time window of tremor bursts. Note that while estimating tremor spectra, we retain the tremor amplitudes in the data. Previous studies using these data suggested the dominance of P waves in the vertical-component records [*Ghosh et al.*, 2009]. However, significant S waves might also be present even in the vertical-component records. We thus carry out the tremor spectral analysis by considering the possibility of S waves as well as P waves. By shooting rays up from the plate interface, we locate the tremor using a plate interface model [*McCrory et al.*, 2004] and a one-dimensional velocity model [*Crosson*, 1976]. The tremor locations generally agree with those shown in previous studies [*Wech and Creager*, 2008; *Ghosh et al.*, 2009].

[9] Seismic records from single stations (Figure 2) normally allow tremor to be observed up to about 10–15 Hz and down to ~1 Hz (Figure 3). Below 1 Hz microseismic energy dominates. Using beamforming we are able to observe tremor as coherent peak energy in beamformer outputs from 2.5 to 25 Hz (Figure 4a). The temporal variation of tremor azimuth indicates a south-to-north migration (Figure 4b). However, simultaneous tremor episodes are often observed at multiple locations. Peak energy as a function of slowness and azimuth (Figure 5) suggests that the tremor is stable and strongest within about 2.5–20 Hz, which we choose as the band for our spectral analysis. Outside of

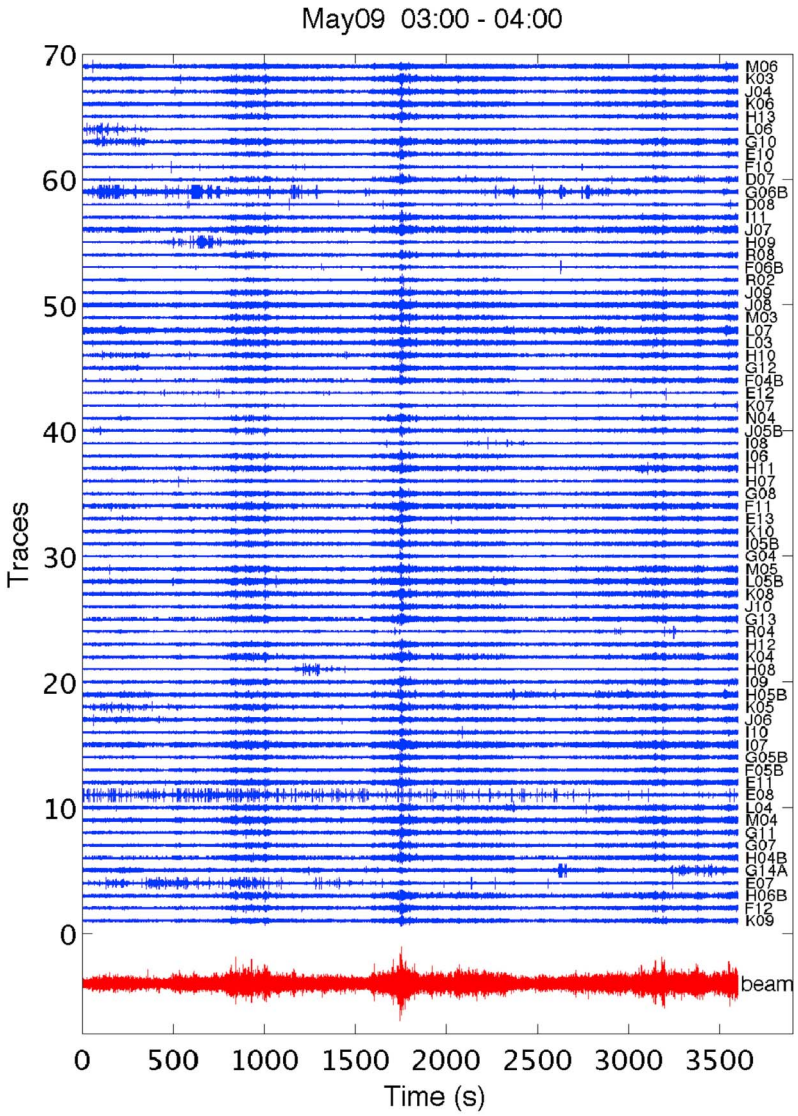

Figure 2. Time series of the tremor bursts during 03:00–04:00 on May 9, 2008, recorded at 69 sensors in the Big Skidder array. The beam (red) is shown in exaggerated scale at the bottom. Note that the tremor is continuously active, not just during the visible high-amplitude portions. Thus the beam shows similar features as individual traces.

this range the noise dominates and so the beamforming resolution is poor.

[10] Although the beamformer peaks represent the strongest tremor phase assuming a point source and ray theory through a layered homogeneous Earth, peak locations (azimuth and slowness) are variable with frequency (Figure 6), likely due to distributed sources, scattering, multipathing, and the possible mix of *P* and *S* wave energy. We have not attempted to resolve how much of this variation is caused by a distributed source versus scattering and other path effects. However, synthetic tests of a distributed source indicate that our spectra estimates from the peak beamformer outputs at each frequency are robust (Figure 7).

[11] Single-station spectra calculations overestimate the signal power at high frequencies where the noise power is comparable to or greater than the signal, and beamforming provides an efficient way to suppress noise. Consider plots of signal and noise strength, as shown in Figure 8a. Using 72 elements of the array we extract both the median of the single-station amplitude estimates and the beam amplitude *S*. At low frequencies the signal dominates and both methods work well, but for higher frequencies where the noise dominates, only the

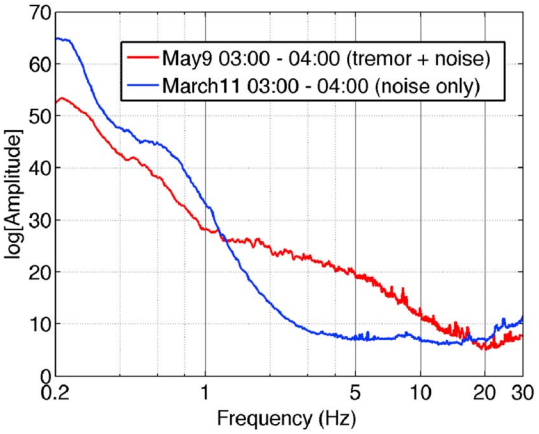

Figure 3. Typical velocity spectra (instrument-response corrected) of tremor plus noise (red) and noise only (blue) averaged over all stations. Below about 1.2 Hz, microseisms are dominating and the spectra rise sharply toward the microseism peak. Potential tremor energy cannot be resolved below 1.2 Hz. Note that the spikes are due to human activities.

beamforming method provides reliable results (Figure 8b).

[12] The tremor amplitude spectrum (displacement, uncorrected for path effects) of the tremor bursts averaged for 3-s intervals during May 9 03:00–04:00 is compared with the median spectral estimates at each individual sensor, and the median noise spectrum from tremor-free data during March 11 03:00–04:00 (Figure 8c). The spectrum estimated from beamforming has a steeper falloff in the 5–20 Hz band, which results from the beamforming correctly suppressing high-frequency noise. Similar observations are shown in Figures 8d and 8e for the other two tremor bursts.

4. Empirical Correction for Path and Attenuation Using Small Nearby Earthquakes

[13] We focus on three tremor bursts (Figures 1a and 9) that are each close to one of three local earthquakes (May 08 h = 8.4 km M_c = 1.4; May 17 h = 52 km M_c = 1.8; May 16 h = 53 km M_c = 1.6, where h is depth; M_c is coda magnitude). Small earthquakes close to the tremor locations can be used to estimate the empirical path term p^2 in equation (4) (Figure 10). In doing so, we take advantage of the study by *Atkinson* [1995], who analyzed earthquake source spectra in this region and solved for a Q model as well as earthquake stress drops. We first model the source spectra of each small earthquake by using the corner frequency f_c. For earthquakes, coda magnitudes are approximately equivalent to local magnitudes, i.e., $M_c \approx M_L$. *Kao et al.* [2010] has found that $M_L \approx M_W$ for earthquakes in Northern Cascadia. Thus the earthquake moment can be estimated using $M_W = \frac{2}{3}(\log_{10} M_0 - 9.1)$ [*Kanamori*, 1977]. f_c can then be estimated using the *Madariaga* [1976] dynamic rupture model: $\Delta\sigma = \frac{7}{16}\left(\frac{f_c}{k\beta}\right)^3 M_0$, where β is shear-velocity, k is 0.32 for the P-wave spectrum, and 0.21 for S waves, given a rupture velocity of 0.9β, and we assume a stress drop of $\Delta\sigma$ = 3 MPa [*Atkinson*, 1995].

[14] We then assume that the displacement amplitude spectrum of the small earthquakes is given by a standard *Brune* [1970] source model $A(f) = \frac{\Omega_0}{1+(f/f_c)^2}$, where Ω_0 is the low-frequency spectral level. This allows an estimate of the empirical path term $p^2 = E(\omega)/A(\omega)$, where $E(\omega)$ is the observed earthquake spectrum measured from a 3-s window of the *P*- or *S*-wave train (Figure 10a). Corrections due to the difference in hypocentral distance (R) of the tremor and earthquake are considered by assuming R^{-1} geometric spreading [*Atkinson*, 1995]. In addition we correct for the depth difference between shallow crustal earthquakes and tremor (Figure 10c) using a Q model [*Atkinson*, 1995] that accounts for the difference between events in the shallow crust and those at the plate boundary ($Q = 174\, f^{0.58}$ for S waves of crustal events and $Q = 263\, f^{0.49}$ for S waves of plate boundary events; Q values for P waves are a factor of 1.4 higher). Although we assume the earthquakes have a typical stress drop of 3 MPa and that their source spectra follow the *Madariaga* model, our results do not depend very much on these assumptions, as we find that changing the assumed stress drops to values from 0.3 to 30 MPa has little effect on the resulting path-effect corrected source spectra (Figure 10d).

5. Tremor Source Spectra

[15] Applying beamforming and empirical path corrections from the nearby earthquakes (Figure 10), we obtain noise-suppressed source spectra at 2.5–20 Hz for the typical tremor bursts, assuming the dominant signals in the records are P waves (Figure 11). Corner frequencies and high-frequency falloff rates are estimated by fitting a standard *Brune*

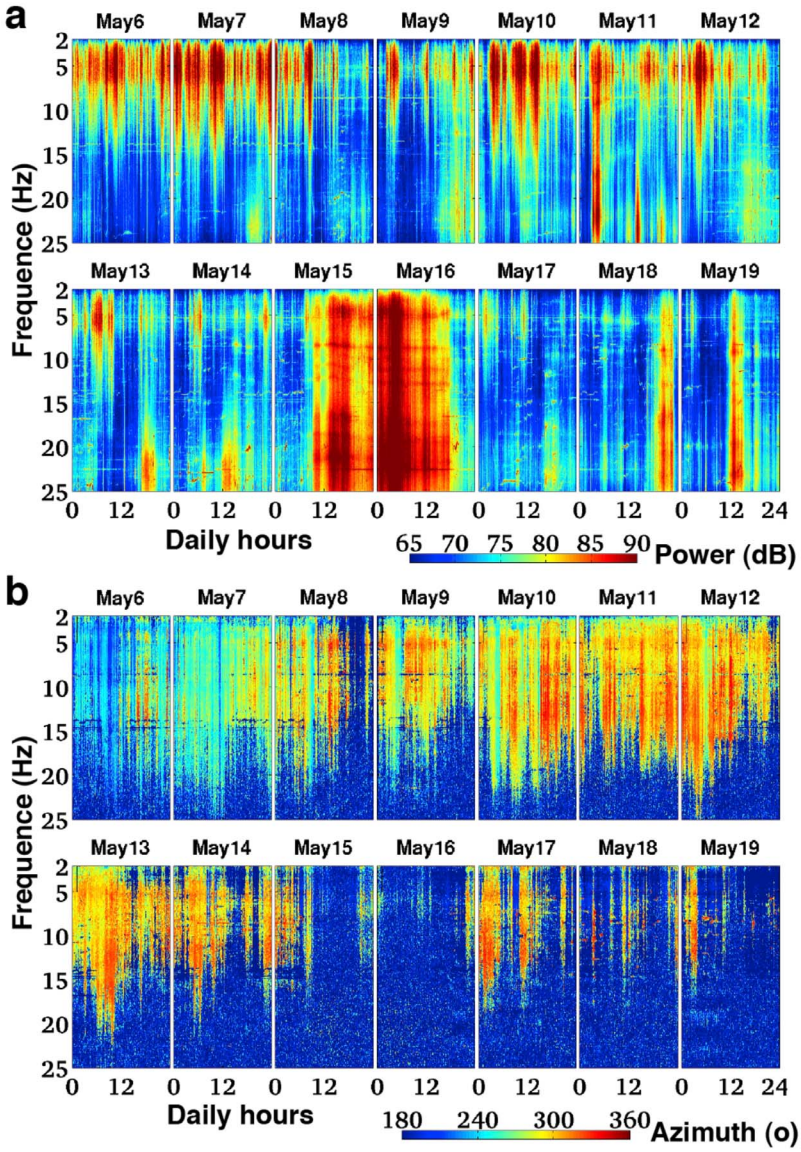

Figure 4. Beamformer outputs. (a) Peak power, and (b) peak azimuth variations (color coded) of the tremor bursts during May 6–19, 2008, as a function of frequency and time. The strong energy from mid May 15 to mid May 16 is rain noise.

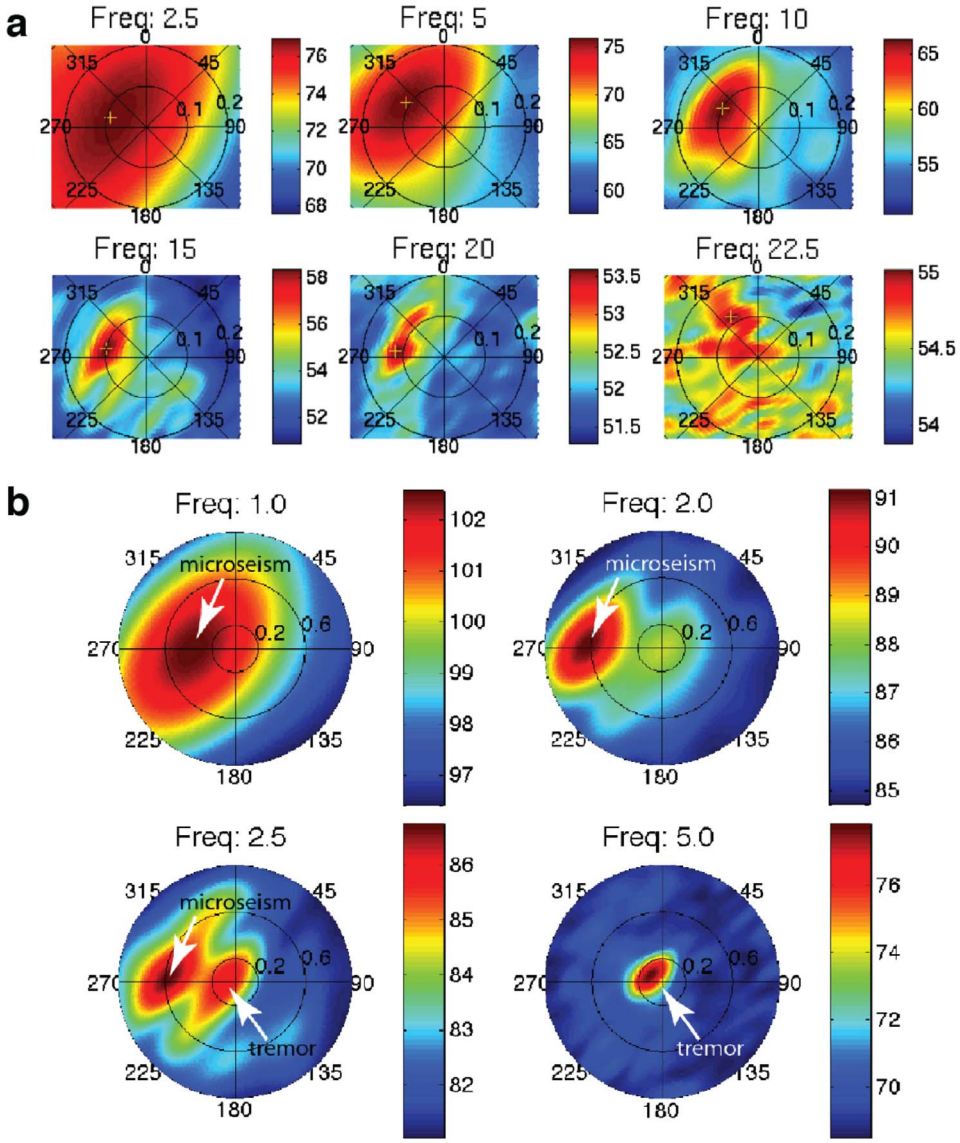

Figure 5. Slowness-azimuth beamformer outputs (0.6-Hz bandwidth for each frequency) for the tremor bursts during May 9 03:00–04:00. (a) Beam of tremor at sampled frequencies. The stable and strongest tremor is band-limited within about 2.5–20 Hz. Resolution is poor for low frequencies and noise dominates for the frequencies outside the 2.5–20 Hz range. (b) Microseism energy dominates the spectrum below 2.5 Hz. Color is coded for power (dB) but each subplot has a different scale.

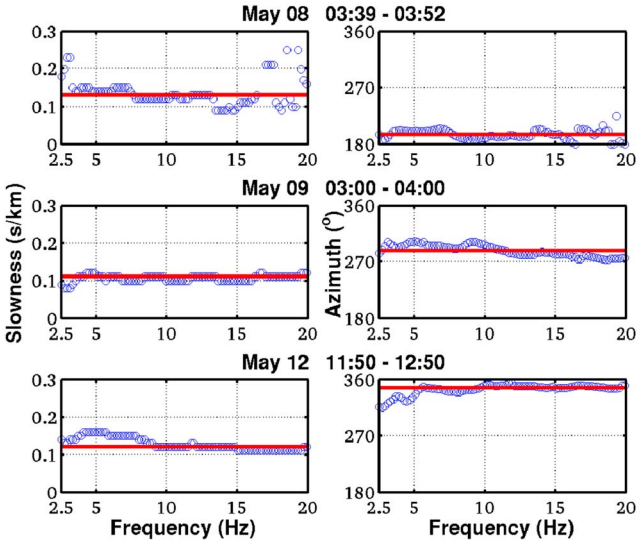

Figure 6. Peak phases (slowness and azimuth respectively) versus frequencies, from the beamformer results for the three tremor bursts in Figure 1. Red lines indicate the medians.

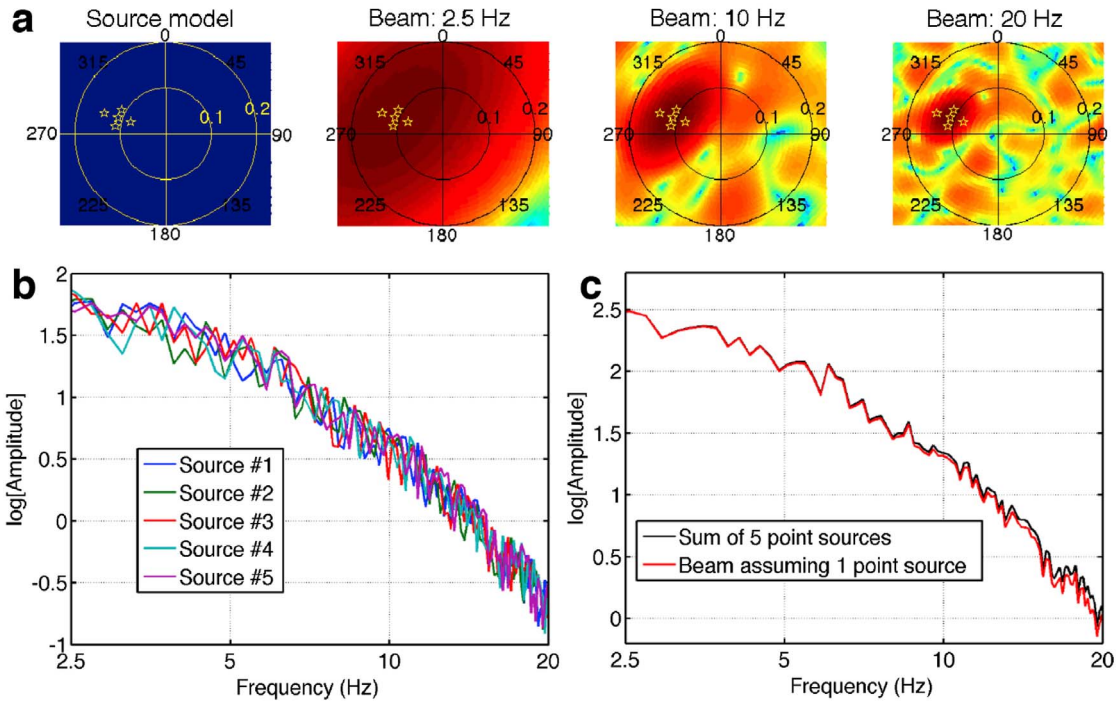

Figure 7. Synthetic test of the point-source assumption. (a) Five point sources (stars) and their plane wave beam at 2.5, 10, 20 Hz; (b) Source spectra of the five point sources; (c) Summed spectra (black) of the five point sources compared with the beam spectrum (red) obtained by assuming a single point source.

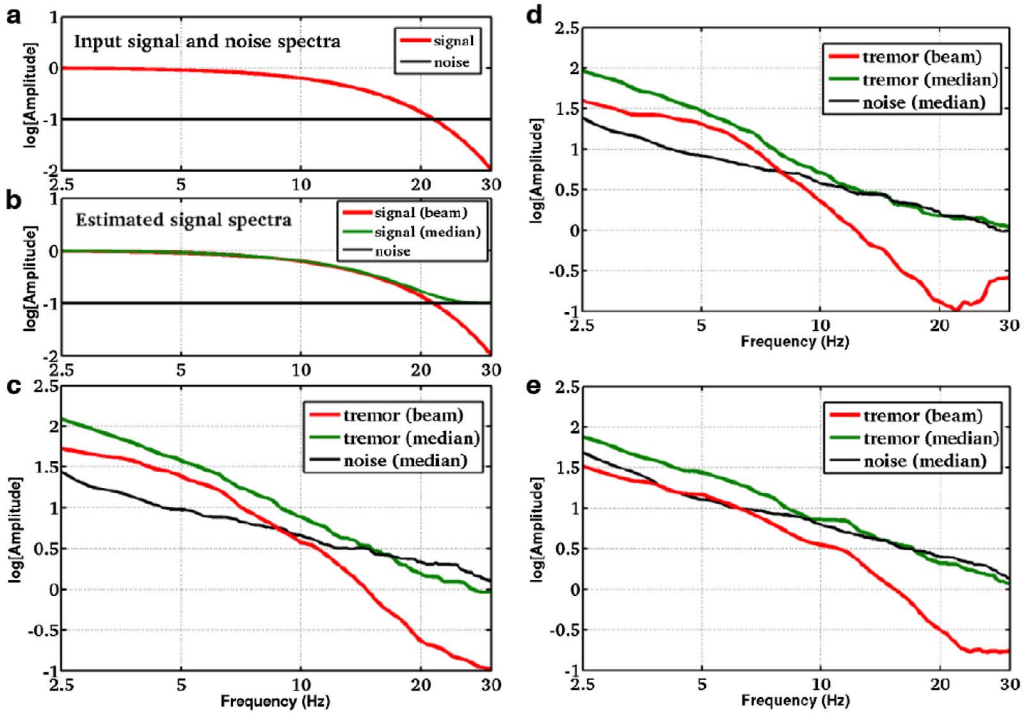

Figure 8. Signal extraction from records with strong high-frequency noise. (a) Simulated signal (red) and noise (black) spectra at each station. (b) Signal strength estimated using beamforming (red), and the median of single-station amplitudes (green). Beamforming estimate (path-effect uncorrected) of typical displacement spectra (average of 3-s intervals) of the Cascadia tremor during (c) May 9 03:00–04:00; (d) May 8 03:39–03:52; and (e) May 12 11:50–12:50 (red) is compared with the median of single-station estimates of the tremor (green), and the median noise amplitude (black) estimated from tremor-free data on March 11, 2008 (same daily hour as the tremor so the cultural noise is similar).

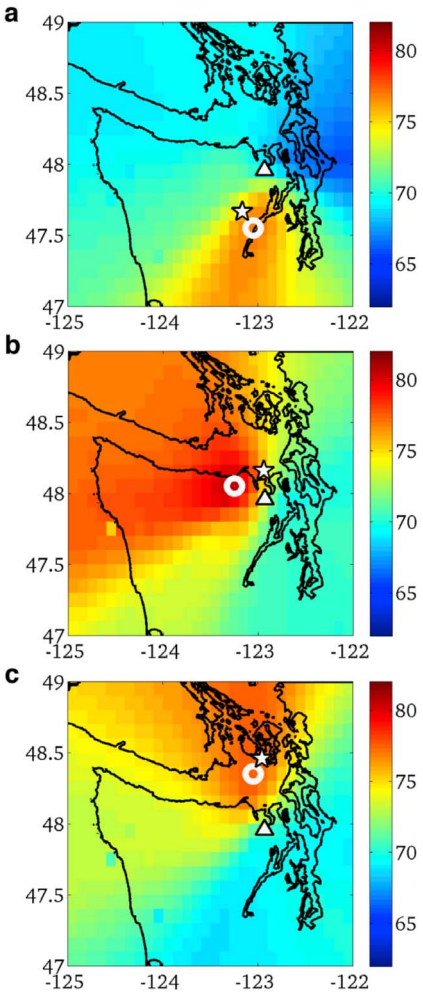

Figure 9. Typical Cascadia tremor locations from beamforming, during (a) May 8 03:39–03:52, (b) May 9 03:00–04:00, and (c) May 12 11:50–12:50. Also shown are the locations of the peak-energy tremor (circle), nearby earthquakes used for empirical path effect analysis (star), and the array (triangle). Color is coded for power (dB).

[1970] model using least squares, with the RMS error less than 0.05 in log[Amplitude]. We then repeat the above analysis by assuming the dominance of *S* waves in the array records. Locations of the three tremor bursts are generally closer to the array than those under the *P*-wave assumption (Figure 12a). Note for the path correction that the third tremor burst is paired with the second earthquake, given that its *S*-wave location is closer to the second earthquake than to the third. Compared with the estimates under the *P*-wave assumption, fitting a *Brune* [1970] model provides similar high-frequency falloff rates and slightly higher corner frequencies (Figure 12b). Here we discard the corner frequency estimate of the third tremor case (f_c = 14.4 Hz) because of the uncertainty due to its step-like spectral shape.

[16] Regardless of wave-type (*P* or *S*), the Cascadia tremor spectra show high-frequency falloff of f^{-2} to f^{-3} that agrees with regular earthquakes. This suggests that tremor can be modeled using standard earthquake source models. However, the Cascadia tremor has much lower corner frequencies (f_c ~3–8 Hz) than would be seen for regular earthquakes producing comparable seismic amplitudes, consistent with tremor being composed of a nearly continuous sequence of low-frequency microearthquakes (LFEs) [*Shelly et al.*, 2006; *Beroza and Ide*, 2011].

6. Discussion

[17] Using the amplitude difference between the tremor and the nearby earthquake (Figures 11 and 12) and assuming $M_c \approx M_L \approx M_W$ (M_c: coda duration magnitude; M_L: local magnitude; M_W: moment magnitude), we can roughly calibrate the tremor moment with the earthquake magnitude. Again the earthquake moment M_0^{eq} can be estimated using $M_W = \frac{2}{3}(\log_{10} M_0 - 9.1)$. For the simple Haskell fault model [e.g., *Shearer*, 2009], the far-field amplitude spectrum for low frequencies is related to the moment as $\log|A(\omega)| = \log M_0 + G$, where G is a scaling term that includes geometrical spreading, which is approximately the same if the earthquake and tremor are close. This gives $\log|A^{tre}(\omega)| - \log|A^{eq}(\omega)| = \log M_0^{tre} - \log M_0^{eq}$.

[18] We thus can use the low-frequency amplitude difference between the tremor and earthquakes (Figures 11 and 12) to estimate the tremor moment M_0^{tre}, which amounts to an average seismic moment release rate of 3.8×10^{10} N·m/s under the *P*-wave assumption, or 1.4×10^{10} N·m/s under the *S*-wave assumption. This is 3 orders of magnitude smaller than the moment release rate calculated by *Aguiar et al.* [2009] from geodetic constraints on the slow slip events that accompany the tremor. Thus while tremor occurs during the slow slip episodes, the tremor process constitutes only a small portion of the total moment release during an ETS event. Assuming tremor moment release is proportional to time, a typical 20-day long tremor episode releases moment equivalent to an Mw = 5.1 event under the *P*-wave assumption, or Mw = 4.9 under the *S*-wave assumption. Note that these may be underestimates if the spectra deviate substantially from the *Brune* [1970] model at very low frequencies.

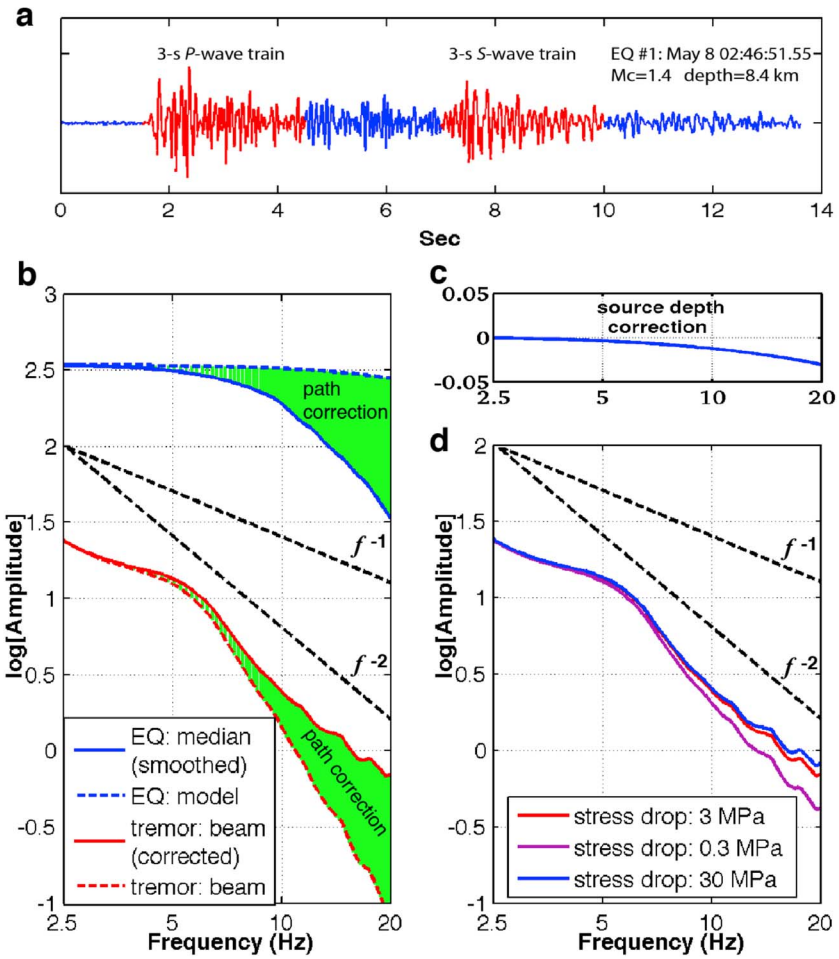

Figure 10. The processing steps for computing the empirical path-effect correction using a small nearby earthquake (M = 1.4, depth = 8.4 km) on May 8, for the tremor bursts during May 8 03:39–03:52 (Figure 9a). (a) Example time series of the earthquake. (b) Using the empirical path-correction (green) from the difference between the smoothed earthquake spectrum (solid blue) and the modeled earthquake source spectrum (dashed blue), the raw tremor spectrum (dashed red) is corrected to the tremor source spectrum (solid red); (c) correction for the difference of attenuation Q for the sources at different depths (tremor: depth = 40 km, assuming it is located at plate interface, and earthquake: depth = 8.4 km); (d) tremor source spectrum with path-effect correction, assuming earthquake stress drop $\Delta\sigma$ of 3 MPa (red), compared with the estimates for $\Delta\sigma$ of 0.3 MPa (magenta) and 30 MPa (blue).

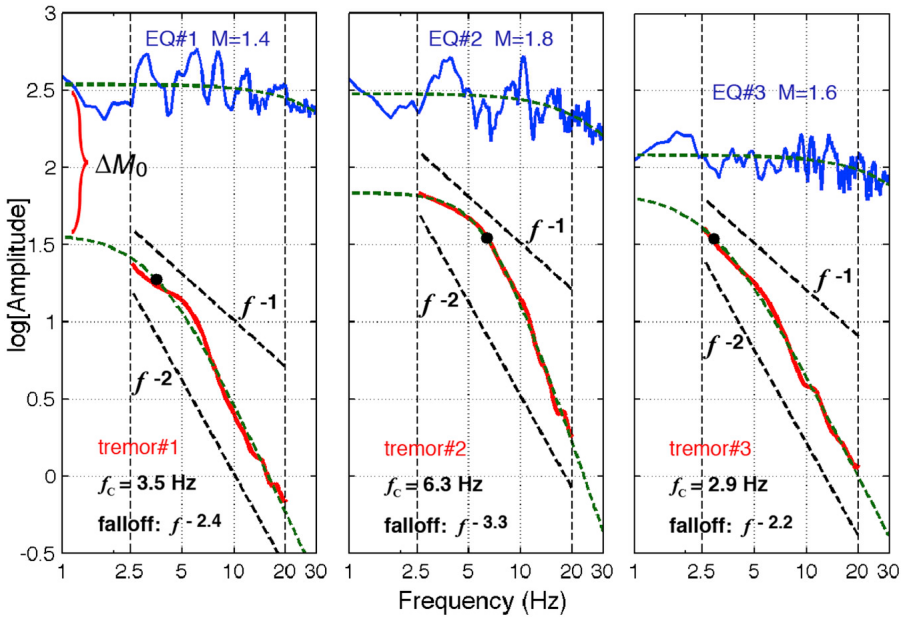

Figure 11. Path-corrected tremor source spectra (solid red) and their best fitting *Brune* [1970] models (dashed green) for three different tremor bursts (average of 3-s intervals) at the locations shown in Figure 1. Black dots show the tremor corner frequencies and the sloping dashed lines show reference f^{-1} and f^{-2} falloff rates. For comparison, the 3-s *P*-wave spectra (solid blue) of three nearby earthquakes and their *Brune* models (dashed green) are also plotted on the same amplitude scale. Note that the earthquakes have both higher amplitudes and higher corner frequencies than the 3-s tremor, and fall off at higher frequencies as f^{-2} (not shown). The low-frequency amplitude difference between the tremor and earthquakes can be used to estimate the tremor moment release rate.

[19] Using the circular crack relation for stress drop as a function of crack radius r [*Eshelby*, 1957], i.e., $\Delta\sigma = \frac{7M_0}{16r^3}$, and assuming each LFE lasts ~1 s, typical earthquake stress drops of 0.3–30 MPa and our estimate of the tremor moment release would result in spectral corner frequencies of 31 to 161 Hz according to the *Madariaga* [1976] dynamic rupture model, i.e., $r = \frac{k\beta}{f_c}$. The much lower corner frequencies of 3–8 Hz that we observe for tremor imply either very low stress drops of 0.2–5 kPa (and r of 105–428 m), or a much slower rupture process than typical earthquakes (the *Madariaga* [1976] model assumes the rupture velocity is 90% of the shear wave velocity). The low tremor stress drops on the order of kPa also agree with the stress drops suggested by Cascadia slow slip models [*Liu and Rice*, 2007; *Rubin*, 2008].

[20] Thus although the tremor spectral falloff implies similarities to the radiated pulse shapes generated by discrete slip events, the physics of the slip process for these tremor events is likely very different from that of regular earthquakes. Based on rate-and-state friction models [e.g., *Liu and Rice*, 2007; *Rubin*, 2008], a low stress drop is suggestive of low effective stress (normal stress minus pore pressure) due to large volumes of hydrous fluids, and thus favored by the evidence of high pore pressures at the plate interface beneath Cascadia [*Peacock et al.*, 2011]. Furthermore, dilatancy stabilization may play an important role controlling the behavior of tremor and/or slow slip [*Segall et al.*, 2010; *Liu and Rubin*, 2010]. This view of tremor as the result of local fine-scale weak faults is also favored by the fact that tremor can be triggered by the small stress changes due to tides and the passage of teleseismic surface waves [*Rubinstein et al.*, 2008, 2009].

7. Conclusions

[21] Spectral characteristics of non-volcanic tremor (NVT) have proven difficult to analyze due to their poor signal-to-noise ratio (SNR). If array data are available, beamforming can be used to suppress noise and allow accurate tremor spectral analysis. By studying the Cascadia tremor recorded at a dense array, we conclude that the displacement spectra of the Cascadia tremor have corner frequencies around 3–8 Hz and fall off at f^{-2} to f^{-3} at higher frequencies.

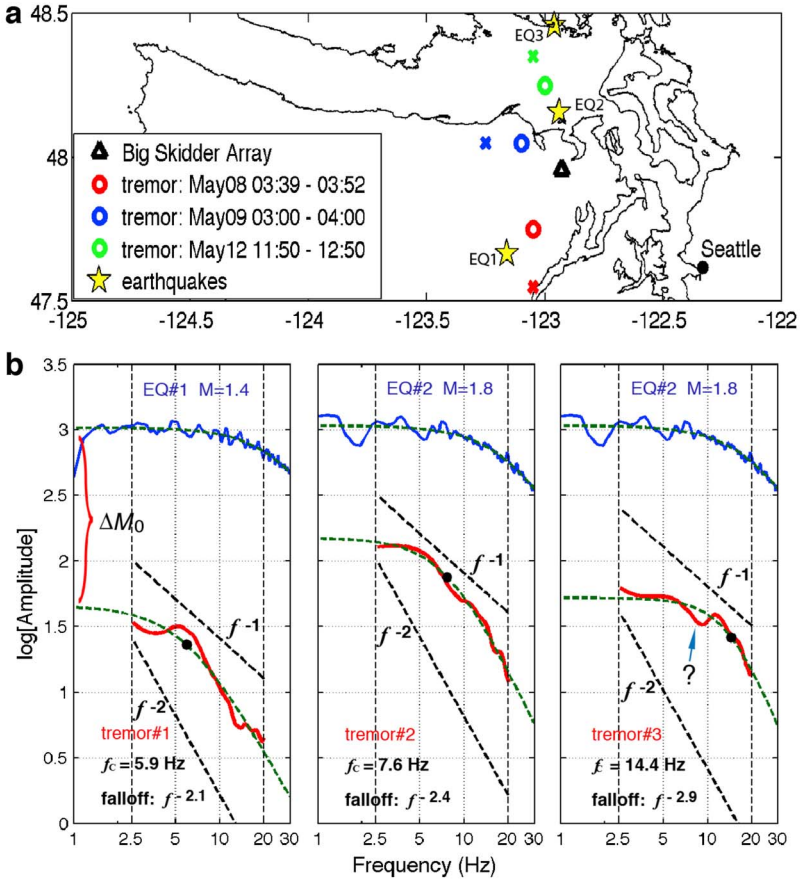

Figure 12. Locations and path-corrected tremor source spectra assuming the dominant signals in the records are *S* waves. (a) Same as in Figure 1, but note the change of locations from those under the *P*-wave assumption (cross) to those under the *S*-wave assumption (circle). (b) Same as in Figure 11, but for spectral estimates assuming *S* waves instead of *P* waves.

[22] The earthquake-like high-frequency falloff suggests that tremor can be studied using standard spectral models for regular earthquakes. Low corner frequencies imply either abnormally small stress drops due to possible high pore pressures (large amount of fluids), or slow ruptures. Fitting a standard *Brune* [1970] spectral model, we infer that a lower bound of moment release rate of Cascadia tremor is 3.8×10^{10} N·m/s assuming the tremor signals we observed are *P* waves, or 1.4×10^{10} N·m/s assuming *S* waves.

Acknowledgments

[23] We thank Thorsten Becker and three anonymous reviewers for their thorough and helpful comments that significantly improved this work. Financial support by the U.S. Air Force Research Laboratory grant FA8718-07-C-0005, and by NSF grants EAR-0710881, EAR-0844392 (Array of Arrays), EAR-0944109, OCE-1030022 is gratefully acknowledged.

References

Aguiar, A. C., T. I. Melbourne, and C. W. Scrivner (2009), Moment release rate of Cascadia tremor constrained by GPS, *J. Geophys. Res.*, *114*, B00A05, doi:10.1029/2008JB005909.

Atkinson, G. M. (1995), Attenuation and source parameters of earthquakes in the Cascadia region, *Bull. Seismol. Soc. Am.*, *85*, 1327–1342.

Beroza, G. C., and S. Ide (2011), Slow earthquakes and nonvolcanic tremor, *Annu. Rev. Earth Planet. Sci.*, *39*, 271–296, doi:10.1146/annurev-earth-040809-152531.

Brooks, T. F., and W. M. Humphreys (2006), A deconvolution approach for the mapping of acoustic sources (DAMAS) determined from phased microphone arrays, *J. Sound Vib.*, *294*, 856–879, doi:10.1016/j.jsv.2005.12.046.

Brune, J. (1970), Tectonic stress and the spectra of seismic shear waves from earthquakes, *J. Geophys. Res.*, *75*, 4997–5009, doi:10.1029/JB075i026p04997.

Crosson, R. S. (1976), Crustal structure modeling of earthquake data: 2. Velocity structure of Puget Sound Region, Washington, *J. Geophys. Res.*, *81*, 3047–3054, doi:10.1029/JB081i017p03047.

Eshelby, J. D. (1957), The determination of the elastic field of an ellipsoidal inclusion, and related problems, *Proc. R. Soc. London, Ser. A*, *241*, 376–396.

Gerstoft, P., P. M. Shearer, N. Harmon, and J. Zhang (2008), Global P, PP, and PKP wave microseisms observed from distant storms, *Geophys. Res. Lett.*, *35*, L23306, doi:10.1029/2008GL036111.

Ghosh, A., J. E. Vidale, J. R. Sweet, and K. C. Creager (2009), Tremor patches in Cascadia revealed by seismic array analysis, *Geophys. Res. Lett.*, *36*, L17316, doi:10.1029/2009GL039080.

Guilhem, A., Z. Peng, and R. M. Nadeau (2010), High-frequency identification of non-volcanic tremor triggered by regional earthquakes, *Geophys. Res. Lett.*, *37*, L16309, doi:10.1029/2010GL044660.

Harmon, N., C. Rychert, and P. Gerstoft (2010), Distribution of noise sources for seismic interferometry, *Geophys. J. Int.*, *183*, 1470–1484, doi:10.1111/j.1365-246X.2010.04802.x.

Ide, S., G. C. Beroza, D. R. Shelly, and T. Uchide (2007), A scaling law for slow earthquakes, *Nature*, *447*, 76–79, doi:10.1038/nature05780.

Kanamori, H. (1977), The energy release in great earthquakes, *J. Geophys. Res.*, *82*, 2981–2987, doi:10.1029/JB082i020p02981.

Kao, H., K. Wang, H. Dragert, J. Y. Kao, and G. Rogers (2010), Estimating seismic moment magnitude (M_w) of tremor bursts in northern Cascadia: Implications for the "seismic efficiency" of episodic tremor and slip, *Geophys. Res. Lett.*, *37*, L19306, doi:10.1029/2010GL044927.

Lee, W. H. K., P. Jennings, C. Kisslinger, and H. Kanamori (Eds.) (2003), *International Handbook of Earthquake & Engineering Seismology*, Part B, 947 pp., Academic, Amsterdam.

Liu, Y., and J. R. Rice (2007), Spontaneous and triggered aseismic deformation transients in a subduction fault model, *J. Geophys. Res.*, *112*, B09404, doi:10.1029/2007JB004930.

Liu, Y., and A. M. Rubin (2010), Role of fault gouge dilatancy on aseismic deformation transients, *J. Geophys. Res.*, *115*, B10414, doi:10.1029/2010JB007522.

Madariaga, R. (1976), Dynamics of an expanding circular fault, *Bull. Seismol. Soc. Am.*, *66*, 639–666.

McCrory, P. A., J. L. Blair, D. H. Oppenheimer, and S. R. Walter (2004), Depth to the Juan de Fuca slab beneath the Cascadia subduction margin: A 3-D model for sorting earthquakes, *USGS DS-91*, U. S. Geol. Surv., Reston, Va.

Obara, K. (2002), Nonvolcanic deep tremor associated with subduction in southwest Japan, *Science*, *296*, 1679–1681, doi:10.1126/science.1070378.

Peacock, S. M., N. I. Christensen, M. G. Bostock, and P. Audet (2011), High pore pressures and porosity at 35 km depth in the Cascadia subduction zone, *Geology*, *39*, 471–474, doi:10.1130/G31649.1.

Peng, Z., and J. Gomberg (2010), An integrated perspective of the continuum between earthquakes and slow-slip phenomena, *Nat. Geosci.*, *3*, 599–607, doi:10.1038/ngeo940.

Rogers, G., and H. Dragert (2003), Episodic tremor and slip on the Cascadia subduction zone: The chatter of silent slip, *Science*, *300*, 1942–1943, doi:10.1126/science.1084783.

Rubin, A. M. (2008), Episodic slow slip events and rate-and-state friction, *J. Geophys. Res.*, *113*, B11414, doi:10.1029/2008JB005642.

Rubinstein, J. L., J. E. Vidale, J. Gomberg, P. Bodin, K. C. Creager, and S. D. Malone (2007), Non-volcanic tremor driven by large transient shear stresses, *Nature*, *448*, 579–582, doi:10.1038/nature06017.

Rubinstein, J. L., M. La Rocca, J. E. Vidale, K. C. Creager, and A. G. Wech (2008), Tidal modulation of non-volcanic tremor, *Science*, *319*, 186–189, doi:10.1126/science.1150558.

Rubinstein, J. L., J. Gomberg, J. E. Vidale, A. G. Wech, H. Kao, K. C. Creager, and G. Rogers (2009), Seismic wave triggering of nonvolcanic tremor, episodic tremor and slip, and earthquakes on Vancouver Island, *J. Geophys. Res.*, *114*, B00A01, doi:10.1029/2008JB005875.

Segall, P., A. M. Rubin, A. M. Bradley, and J. R. Rice (2010), Dilatant strengthening as a mechanism for slow slip events, *J. Geophys. Res.*, *115*, B12305, doi:10.1029/2010JB007449.

Shearer, P. M. (2009), *Introduction to Seismology*, 2nd ed., Cambridge Univ. Press, New York.

Shelly, D. R., G. C. Beroza, S. Ide, and S. Nakamula (2006), Low-frequency earthquakes in Shikoku, Japan, and their relationship to episodic tremor and slip, *Nature*, *442*, 188–191, doi:10.1038/nature04931.

Shelly, D. R., G. C. Beroza, and S. Ide (2007), Non-volcanic tremor and low frequency earthquake swarms, *Nature*, *446*, 305–307, doi:10.1038/nature05666.

Wech, A. G., and K. C. Creager (2008), Automated detection and location of Cascadia tremor, *Geophys. Res. Lett.*, *35*, L20302, doi:10.1029/2008GL035458.